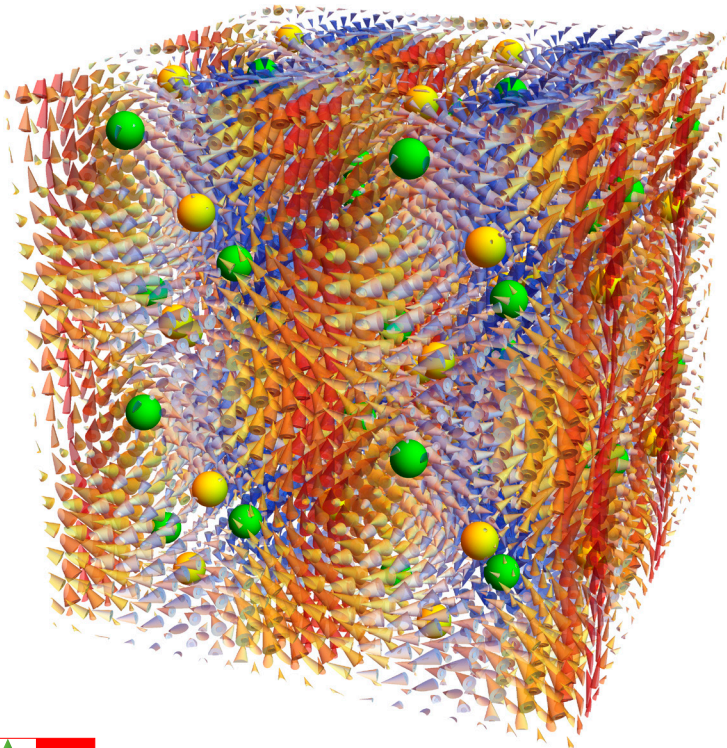


Number 58 | November 2021

SWISS NEUTRON NEWS



Schweizerische Gesellschaft für Neutronenforschung
Société Suisse de la Science Neutronique
Swiss Neutron Science Society

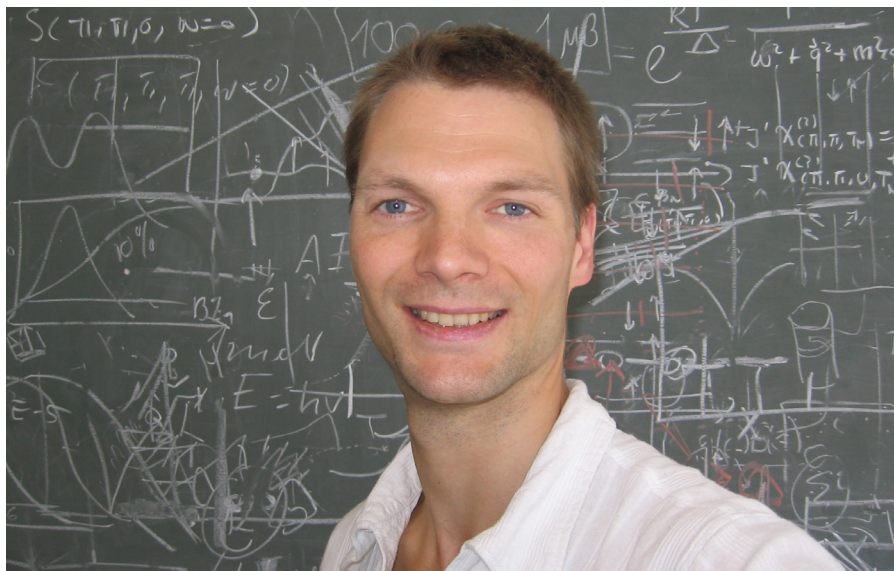
**On the cover**

Schematic of the cubic magnetic hedgehog lattice in MnGe, see the related article "Direct Observation of the Statics and Dynamics of Emergent Magnetic Monopoles in a Chiral Magnet" by J.S. White, N. Kanazawa, A. Kitaori, V. Ukleev, H.M. Rønnow, and Y. Tokura.

Contents

- 4** The President's Page
- 5** Direct Observation of the Statics and Dynamics of Emergent Magnetic Monopoles in a Chiral Magnet
- 16** Polarization Analyzed Imaging with a Neutron Grating Interferometer
- 24** Announcements
- 26** Winners of the Young Scientist Prize 2021 of the Swiss Neutron Science Society, sponsored by SwissNeutronics
- 27** Young Scientist Prize 2022 of the Swiss Neutron Science Society, sponsored by SwissNeutronics - Call for Nominations
- 28** Conferences and Workshops
- 31** Editorial

The President's Page



Dear fellow neutron scientists,

Welcome to this issue of Neutron news, where you will be able to read two magnificent examples of just how sophisticated neutron techniques are becoming - on one hand making it possible to identify complex textures of the electronic spins in materials, on the other hand using the spin of the neutron for polarized neutron imaging experiments.

In addition to the article, you will be able to hear Jacopo Valsecchi speak about the polarized neutron imaging technique at the general assembly of the Swiss Neutron Sci-

ence Society on November 26th. Likewise at this general assembly will be the election of my successor as president of the society. I would therefore like to take this opportunity to thank all the many colleagues within Switzerland and beyond, whom I have had the pleasure of interacting with in this role, and to thank all neutron scientists, who make this field of research so lively and inspiring.

A bientot
Henrik

Direct Observation of the Statics and Dynamics of Emergent Magnetic Monopoles in a Chiral Magnet

Jonathan S. White ^{1*}, Naoya Kanazawa ^{2*},
Aki Kitaori ², Victor Ukleev ¹,
Henrik M. Rønnow ³, Yoshinori Tokura ^{2,4,5}

¹Laboratory for Neutron Scattering and Imaging, Paul Scherrer Institut, 5232 Villigen PSI, Switzerland.

²Department of Applied Physics, University of Tokyo, Tokyo 113-8656, Japan

³Laboratory for Quantum Magnetism, Institute of Physics, École Polytechnique Fédérale de Lausanne (EPFL), 1015 Lausanne, Switzerland

⁴RIKEN Center for Emergent Matter Science (CEMS), Wako 351-0198, Japan

⁵Tokyo College, University of Tokyo, Tokyo 113-8656, Japan

*email: jonathan.white@psi.ch,
kanazawa@ap.t.u-tokyo.ac.jp

After: N. Kanazawa†, A. Kitaori†, J.S. White†
et al., Phys. Rev. Lett. **125** 137202 (2020)

Abstract

In nature, free magnetic monopoles remain elusive, and their search, particularly in high-energy physics, is an ongoing challenge. In contrast, construction of the monopole solution ($\propto \mathbf{r}/|\mathbf{r}|^3$) is possible by manipulating the electronic and spin textures in Condensed Matter systems, as exemplified by liquid crystals, spin ices, chiral magnets, and others. One strategy to create such ‘emergent monopoles’ is to utilize topological defects or orders that yield quantized Berry phase, the latter amounting to a quantized source or sink of effective gauge field called an ‘emergent magnetic field’. While expected to exist in real systems, the dynamics and novel electromagnetic responses of such emergent monopoles remain largely unexplored. Here we combine small-angle neutron scattering and electrical transport to explore the static and dynamic properties of emergent monopole crystals created by mode-coupling three orthogonal spin helices in single crystalline samples of the chiral-lattice magnet MnGe. In the static limit, the magnetic structure generating the monopole crystal models well both the neutron diffraction data and the averaged static emergent magnetic field that appears as a topological Hall effect. Augmenting the spin fluctuations upon increasing the

magnetic field and/or temperature invokes the dynamics of emergent monopole fields, which are manifested as diffusive small-angle neutron diffraction patterns, and strong skew scattering that leads to a remarkable sign reversal of the Hall effect. Our approach of combining neutron scattering and transport measurements on single crystal samples of MnGe provides an original exploration of the static and dynamic properties of magnetic monopole crystals, and paves the way for the discovery of further versatile phenomena due to emergent monopoles and their coupling with itinerant electrons.

Emergent Monopoles and Hedgehogs in Condensed Matter

Artificial monopole structures have been proposed and indeed realized in Condensed Matter in different ways. Well-known examples include the spin ices, wherein highly-frustrated Ising spins on the pyrochlore lattice form a so-called two-in/two-out magnetization configuration with a divergence-free magnetization ($\nabla \cdot \mathbf{M} = 0$) at every local point. Spin-flip excitations cause imbalances of local magnet-

ization that behave as magnetic point defects with a divergent solution of \mathbf{H} -field, thus providing the opportunity to examine analogues of magnetic monopoles [1]. In a similar way, defects in an ordered system have potential to become singularities in classical and/or quantum fields, thus acting as monopole-like objects. A good example are point charge defects in linear magnetoelectrics. Here, the divergence of the electric field from the point charge is converted to magnetization via the linear cross-correlation relation $\mathbf{M} = \alpha \mathbf{E}$ [2].

In particular, when a defect in a solid possesses nontrivial topology, the corresponding field singularity can become quantized, analogous to the original magnetic monopole introduced by Dirac [3]. Such defects are, for example, hedgehog-type spin structures coupled with conduction electrons in magnetic metals. Spin hedgehogs describe not only a literal spin structure, i.e., spins pointing inwards or outwards from a singular point with zero spin amplitude as shown schematically in Figures 1(a) and (b), but also other structures with integer topological charges described by the winding number $w = \frac{1}{8\pi} \epsilon^{ijk} \int_S dS_k \mathbf{n}(\mathbf{r}) \cdot [\partial_i \mathbf{n}(\mathbf{r}) \times \partial_j \mathbf{n}(\mathbf{r})] = \pm 1$ [4]. This quantity represents the mapping of the order parameter $\mathbf{m}(\mathbf{r})$ on to the sphere S that surrounds the singular point in real space, to the sphere of the unit vector with

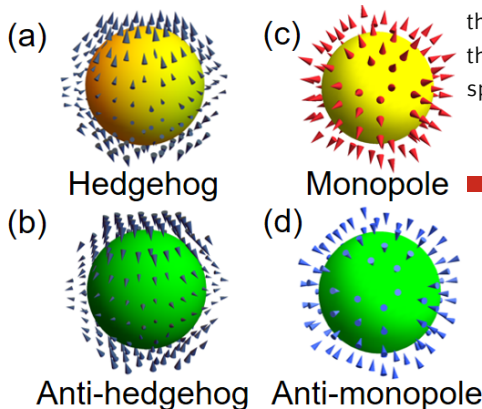


Figure 1

Schematics of (a) spin hedgehog and (b) spin anti-hedgehog spin structures. The associated monopolar emergent magnetic field distributions for the spin structures shown in (a) and (b) are respectively shown in panels (c) and (d).

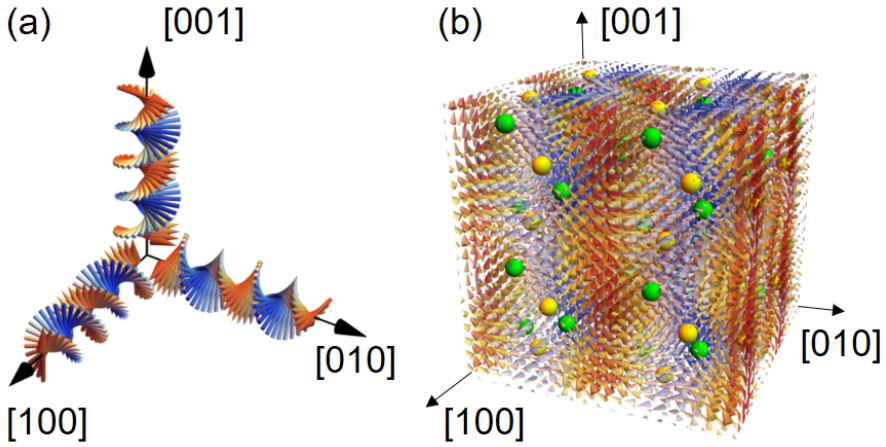


Figure 2

Construction of a monopole crystal ground state in MnGe. (a) Schematic indicating three orthogonal helical structures propagating along the cubic axes. The superposition of the three helices forms the cubic hedgehog lattice state in MnGe shown in (b). In (b) reddish and bluish arrows indicate spins with positive and negative z components, respectively. The yellow and green dots denote regions where hedgehog and antihedgehog spin structures [like those shown in Figures 1(a) and (b)] generating emergent monopolar fields [like those shown in Figures 1(c) and (d)] can be found.

direction $\mathbf{n}(\mathbf{r}) = \mathbf{m}(\mathbf{r}) / |\mathbf{m}(\mathbf{r})|$. Meanwhile, the conduction electrons sense the spatially-dependent spin-tilting direction as the Berry curvature $b_k = \frac{1}{2} \epsilon^{ijk} \mathbf{n}(\mathbf{r}) \cdot [\partial_i \mathbf{n}(\mathbf{r}) \times \partial_j \mathbf{n}(\mathbf{r})]$, which corresponds to an effective gauge field, i.e., an emergent magnetic field affecting electron motion in the same manner as a classical magnetic field [5]. Conduction electrons therefore regard spin hedgehogs as quantized sources or sinks of emergent monopolar fields with effective magnetic charge $Q_m = \frac{1}{4\pi} \int_S dS_k b_k = \pm 1$, as illustrated in Figures 1(c) and 1(d).

In a static crystal of spin hedgehogs and hence of emergent monopoles, oppositely-charged hedgehogs are connected by quan-

tized lines of emergent magnetic field that strongly deflect conduction electrons. This gives rise to a distinct contribution to the Hall effect, known as the topological Hall effect (THE) [6-7]. The dynamical behaviour of emergent monopoles is far more difficult to detect in transport, since the fluctuations of the emergent magnetic field that scatter electrons are expected to lead only to small voltage noise. Instead, it is expected that steady Hall signals due to emergent monopoles dynamics can be generated when the associated spin fluctuations themselves display a finite thermally averaged total chirality, as can be achieved through a preferential selection of certain chiral fluctuation modes [8]. This sit-

uation can be realised in chiral magnetic materials that lack spatial inversion symmetry, and in which a homochiral nature of spin fluctuations is expected.

To search for observable manifestations of the statics and dynamics of emergent monopoles in a single system, we targeted the chiral cubic magnet MnGe, which realises a periodic crystal of spin-hedgehogs (monopoles) and antihedgehogs (antimonopoles) as the magnetic ground state [9-11]. Figure 2 illustrates the construction of the monopole-antimonopole crystal in MnGe through the coherent superposition of three proper screw helical modulations propagating along the cubic axes, forming a so-called triple- q structure.

Single crystalline samples of MnGe

Previous neutron experiments on powder samples shows the magnetic modulation period in MnGe varies between 3-6 nm as functions of both magnetic field and temperature below the magnetic transition temperature $T_N \sim 170$ K [11-13]. However, the more detailed study of the magnetism and the monopole dynamics were not possible to date due to a lack of single crystal samples. To overcome this challenge, in the present work, two different approaches have been adopted. Namely, a high pressure synthesis approach yielding bulk single crystals of lateral size $\sim 50\mu\text{m}$ suitable for transport, and the growth of large area, single crystalline films by molecular beam epitaxy, suitable for neutron scattering measurements. Figure 3(a) shows a $3\mu\text{m}$ thick MnGe film deposited onto a 2-inch diameter Si(111) substrate. By growing films of μm thickness, the film is always many

hundreds of times larger than the modulation period, thus promoting bulk magnetic behaviour and suppressing the influences of surface and interface effects. For the neutron experiments, two pieces were cut to size from a single wafer, co-aligned and mounted into a bespoke sample holder. The holder, shown in Figure 3(b), was designed to be suitable for installation into a beamline cryomagnet sample environment. An important aspect of the epitaxial film growth along the [111] direction is the equal probability for the nucleation of two crystalline domains with opposite structural chirality [14]. These two domains are related by a mirror operation with respect to the (111) plane. As schematically illustrated in Figures 3(c) and (d), the corresponding pattern of magnetic Bragg peaks observed experimentally from the film is thus expected to be six-fold symmetric around the [111] direction due to contributions from triple- q hedgehog-antihedgehog lattices in each structural domain, rather than just the threefold symmetric pattern expected from a single structural domain sample.

Characterizing multi- q magnetic order by SANS

The small-angle neutron scattering (SANS) instrument geometry with two-dimensional multidetector placed behind the sample provides full flexibility for the versatile study of the magnetic field- and temperature-dependence of the magnetic Bragg scattering from the MnGe thick film. Figure 4(a) shows an aerial schematic of the experimental geometry with no magnetic field. In this case, the sample is freely rotatable (or ‘rocked’) around the vertical axis, allowing all magnetic scat-

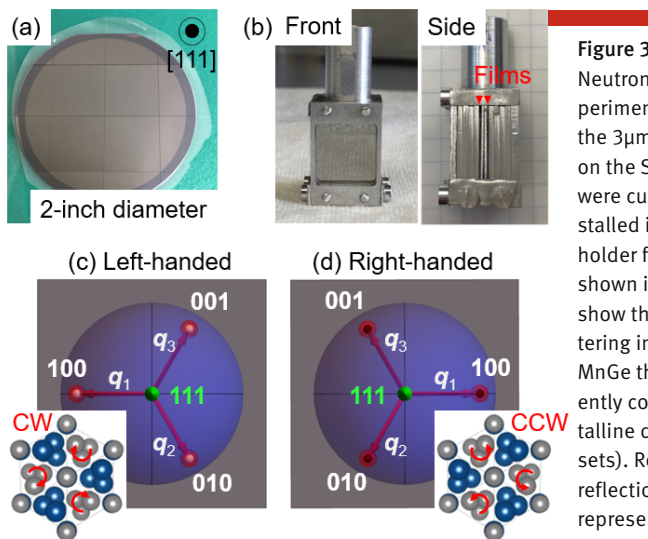


Figure 3

Neutron sample synthesis and experiment details. (a) Aerial view of the $3\mu\text{m}$ thick MnGe film deposited on the Si(111) substrate. Two pieces were cut from the wafer and installed into the bespoke sample holder for neutron experiments shown in panel (b). (c) and (d) show the expected neutron scattering intensity maps from the MnGe thick film, which are inherently composed of two chiral crystalline domains (illustrated as insets). Red dots represent magnetic reflections. White and black dots represent $\langle 100 \rangle$ axes from the left- and right-handed domains, respectively. In the experiment, the scattering from both chiral crystal domains illustrated in (c) and (d) is observed simultaneously.

tering peaks to move through their Bragg condition at the detector. By performing detector measurements at each rotation angle, intensity maps like those shown in Figure 4(b) are constructed, which represent the intensity on a sphere in reciprocal space of radius $|q|$, where $|q|$ denotes the length of the fundamental magnetic propagation vectors. Figure 4(b) shows the intensity map constructed from data collected from MnGe in zero field, and at 2K, this showing good agreement with that expected by combining the intensity maps from hedgehog lattices in each of the crystalline domains indicated in Figure 3(c) and (d).

In a finite magnetic field, the sample orientation with respect to the magnetic field direction must remain fixed, and portions of reciprocal space cannot be studied due to restrictions on neutron beam access imposed by the cryomagnet construction. Figures 4(c) and (d) illustrate the effect of restricted access that obscure certain regions of reciprocal space. Nonetheless, it is still possible to de-

duce the distribution of magnetic intensity from the imaged regions. Figure 4(d) shows the intensity map obtained at 2K and in a magnetic field of 6T applied along the [111] direction. Compared with at zero field [Figure 4(b)], the intensity map is strongly modified, and the magnetic propagation is tilted towards the applied field direction.

SANS investigation of the statics and dynamics of emergent monopoles in MnGe

To study the magnetic static and dynamic monopolar regime in the thick film MnGe sample, we used SANS to characterize the magnetic diffraction peaks due to the multi- q hedgehog lattice as functions of temperature and magnetic field applied along the [111]

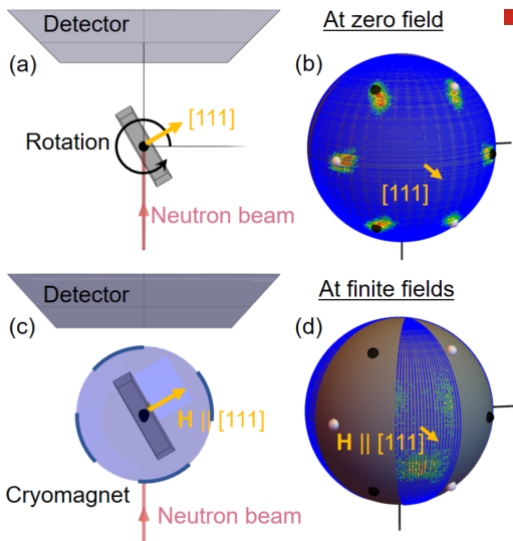


Figure 4

Overview of SANS technique for studying the magnetism in the thick MnGe film. (a) Aerial schematic of the experimental setup for studying the magnetism in the film for zero field. In zero field, detector measurements performed for a full range of sample rotation angles allow construction of the intensity map shown in (b), which reveals the magnetic Bragg scattering due to the multi- q magnetic ground-state at 2 K. (c) Aerial schematic of the setup where the sample is in a cryomagnet, and the direction of the magnetic field is fixed with respect to the sample orientation. Due to parts of the magnet construction that block the beam, not all of reciprocal space can be studied. For a magnetic field of 6T applied along the

[111] direction of the MnGe films, panel (d) shows the intensity map at 2K with both the imaged and obscured regions of reciprocal space. From the visible part of the map, the intensity distribution is clearly modified with respect to zero field.

direction. In Figure 5 a selection of SANS scattering patterns with accompanying schematic illustrations are shown in panels 5(a)-(f), along with quantitative determinations of diffraction spot positions [Figures 5(g)-(i)] and estimations of the area sizes of the SANS diffraction spots [Figures 5(j)-(l)]. In zero magnetic field, Figures 5(a)-(c) show that we observe the expected sixfold symmetric pattern of magnetic peaks due to cubic hedgehog lattice formation up to $T = 100$ K. By inspection, it is clear that the spot sizes are larger at 100 K than at 2 K or 50 K, with this supported from a quantitative evaluation of the spot area shown in Figures 5(j)-(l). This denotes a strong temperature-dependence of the magnetic correlation length at temperatures far below $T_N \sim 170$ K, with the increased spatial disorder (i.e. spot size) at higher tem-

peratures a consequence of thermally-induced temporal spin fluctuations. At lower temperatures below ~ 30 -50 K, when temporal spin fluctuations finally freeze out, the residual spread in width of the magnetic Bragg peaks is due to the static disorder of the hedgehog lattice.

As shown in Figures 5(d)-(f), increasing the magnetic field causes the three propagation vectors of the hedgehog lattice to tilt from an alignment with $\langle 100 \rangle$ towards the field direction. The magnetic diffraction spots from each crystalline domain tend towards overlapping, resulting in scattering patterns that are threefold symmetric around the [111] axis; see for example Figure 5(e) with $T = 50$ K and $\mu_0 H = 6$ T. The tendency towards a threefold symmetric scattering pattern is observed too at $T = 2$ K and $\mu_0 H = 8$ T where much of reciprocal space

hedgehog motion must be induced at the transition. Such a large field-driven deformation of the hedgehog lattice likely enhances hedgehog dynamics, resulting in diffuse scattering patterns observed under finite field at both $T = 50$ and 100 K.

Connection between the magnetic state and the Hall response

Finally, we reveal the connection between the magnetic states studied by SANS and the associated signatures in electrical transport. To this end, the transverse Hall resistivity ρ_{yx} was measured on the bulk single crystal of MnGe with micron dimensions prepared by high pressure synthesis. An SEM image of such a crystal is shown as the inset to Figure 6(a). It is worth mentioning that the successful synthesis of bulk MnGe single crystals of sufficient size for transport was a long-standing challenge overcome in the present work.

From magnetic field dependent measurements of ρ_{yx} , ‘additional’ Hall contributions beyond standard responses due to the normal and anomalous Hall effects are observed at all temperatures below T_N . A full account of these data is given in our original publication [15], and they reveal a clear sensitivity of ρ_{yx} to the static or dynamic state of the hedgehog lattice. For brevity here, we focus only on the magnetic field-dependence of the additional contributions to the Hall effect, which are collectively denoted as ρ_{yx}^T , this being the usual notation for a topological Hall effect (THE) generated by magnetic entities with a non-trivial real-space topology, such as hedgehogs and skyrmions.

Figure 6(a) shows the magnetic field-dependence of ρ_{yx}^T at various temperatures. In

the low temperature region below 20 K, where the hedgehog lattice is static, ρ_{yx}^T displays a broadly negative signal with a small positive bump denoted by the black arrow, and then rises sharply with the increase of the field toward saturation at the critical field H_c . At the higher temperature of $T = 50$ K, where SANS reveals fluctuations of the hedgehog lattice to be introduced under the applied field, ρ_{yx}^T is negative at low field, followed by a large peak at around 6 T, and at higher fields ρ_{yx}^T remains positive up to saturation. A similar behaviour is seen at 100 K, where pronounced fluctuations of the hedgehog lattice exist even in zero field. Overall, as the temperature increases, the negative sign of ρ_{yx}^T observed across the whole field range below 20 K becomes confined to a smaller field region, and an increasingly pronounced positive ρ_{yx}^T peak instead dominates the response.

In Figure 6(b) we show a phase diagram that summarises the correlation between the magnetic field-dependent ρ_{yx}^T data (the colourmap) and the SANS data. From this phase diagram we deduce that the emergence of a positive ρ_{yx}^T correlates with the onset of either magnetic field- or temperature-induced fluctuations of the hedgehog lattice. In addition, the field of the positive peak in ρ_{yx}^T , denoted H_p in Figure 6(a), is found to correlate with a sharp change in propagation vector alignment denoted by H_t in Figures 5(g)-(i). Crucially, ρ_{yx}^T is seen to be positive in regions with pronounced fluctuations of the hedgehog lattice, i.e. where cyan, orange and yellow symbols in Figure 6(b) indicate diffusive magnetic scattering patterns observed by SANS. In contrast, a negative ρ_{yx}^T is observed in the low temperature region, where correspondingly the blue and red symbols in Figure 6(b) denote

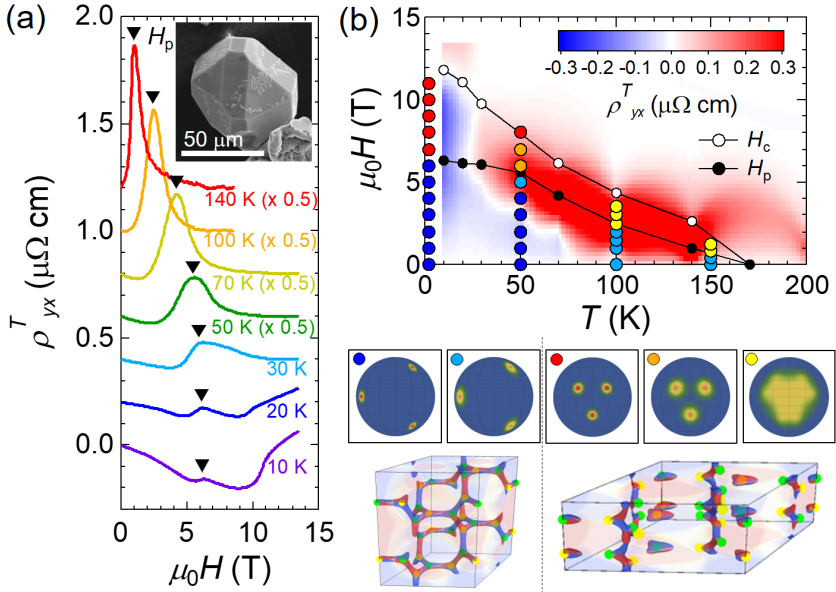


Figure 6

Connection between unconventional Hall responses and the magnetic state in single crystal MnGe. (a) Magnetic field- and temperature-dependence of ρ_{yx}^T obtained on a single crystal sample like that shown in the inset. Data at adjacent temperatures are shifted vertically for clarity. Black triangles denote the magnetic fields H_p at the tops of positive peak structures. (b) Indicative colour map of ρ_{yx}^T

plotted with a scatter plot of the SANS pattern type across the MnGe phase diagram, along with critical fields H_p and H_c . Different colour markers shown in the middle row of panels indicates each different category of SANS pattern classified according to both the directions and the diffuseness of the scattering spots. The bottom panels show the distributions of hedgehogs (yellow dots), antihedgehogs (green dots) and emergent magnetic field (reddish and bluish regions) within the respective magnetic unit cells of the cubic (bottom left) and rhombohedral (bottom right) hedgehog lattices.

SANS data whereby the magnetic scattering signal is concentrated into well-defined peaks due to the static hedgehog lattice.

By combining the SANS and transport data, we deduce that the static and dynamic properties of the hedgehog lattice each likely generate unconventional Hall effects that are distinguished by their opposite sign. Previous

work [11,16] has shown that a negative ρ_{yx}^T can be assigned to a genuine THE induced by the emergent magnetic field distributions for both cubic and rhombohedral types of static hedgehog lattice in MnGe [visualised in the bottom panels of Figure 6(b)]. On the other hand, the onset of a positive ρ_{yx}^T can be understood in theory as caused by the skew scattering of

conduction electrons due to the augmented fluctuations of the correlated spin state with finite scalar spin chirality [8]. These two scenarios explaining regimes described by opposite signs of ρ_{yx}^T , are exemplified in the present case for MnGe in terms of the static and dynamic regimes of the hedgehog lattice.

Importance

The experimental distinction between the static and dynamic properties of emergent monopoles in an archetypal itinerant chiral magnet MnGe has been achieved through a combination of neutron diffraction in the SANS geometry and electrical transport measurements. Each of these experiments were done for the first time on novel single crystalline samples. Notably, the augmentation of spin-chirality fluctuations with either temperature or magnetic field leads to transformative aspects of the SANS data, and the generation of a steady Hall response which is of opposite sign to that due to the static emergent magnetic field distribution of the hedgehog lattice groundstate. The appearance of unusual Hall anomalies is not restricted to hedgehog lattices, and it is a general phenomenon associated with non-coplanar and topological magnetic structures. Correspondingly, our experimental approach proves ideal for establishing the both the static and dynamic properties of topological magnetic textures presently being discovered across an increasingly diverse array of magnetic systems.

Acknowledgements

We thank A. Tsukazaki, M. Ichikawa and M. Kawasaki for their contribution to the present work, and acknowledge the allocation of neutron beamtime at the Swiss Spallation Neutron Source (SINQ), Paul Scherrer Institute (PSI), Villigen, Switzerland. This work was supported by JSPS KAKENHI (Grants No. JP18K13497, No. JP20H01859, No. JP20H05155, and No. JP20H01867), JST CREST (Grant No. JPMJCR16F1 and No. JPMJCR1874), the Swiss National Science Foundation (SNSF) Sinergia network “NanoSkyrmionics” (Grant No. CRSII5_171003), the SNSF Projects No. 200021_188707 and No. 166298, and the European Research Council Project CONQUEST.

References

- [1] C. Castelnovo, R. Moessner, and S. L. Sondhi, *Nature (London)* **451**, 42 (2008).
- [2] D.I. Khomskii, *Nat. Commun.* **5**, 4793 (2014).
- [3] P. A. M. Dirac, *Proc. R. Soc. A* **133**, 60 (1931).
- [4] N. D. Mermin, *Rev. Mod. Phys.* **51**, 591 (1979).
- [5] N. Nagaosa and Y. Tokura, *Phys. Scr.* **T146**, 014020 (2012).
- [6] J. Ye, Y. B. Kim, A. J. Millis, B. I. Shraiman, P. Majumdar, and Z. Tešanović, *Phys. Rev. Lett.* **83**, 3737 (1999).
- [7] P. Bruno, V. K. Dugaev, and M. Taillefumier, *Phys. Rev. Lett.* **93**, 096806 (2004).
- [8] H. Ishizuka and N. Nagaosa, *Sci. Adv.* **4**, eaap9962 (2018).
- [9] N. Kanazawa, Y. Nii, X.-X. Zhang, A. S. Mishchenko, G. De Filippis, F. Kagawa, Y. Iwasa, N. Nagaosa, and Y. Tokura, *Nat. Commun.* **7**, 11622 (2016).
- [10] T. Tanigaki, K. Shibata, N. Kanazawa, X. Z. Yu, Y. Onose, H. S. Park, D. Shindo, and Y. Tokura, *Nano Lett.* **15**, 5438 (2015).
- [11] N. Kanazawa, Y. Onose, T. Arima, D. Okuyama, K. Ohoyama, S. Wakimoto, K. Kakurai, S. Ishiwata, and Y. Tokura, *Phys. Rev. Lett.* **106**, 156603 (2011).
- [12] N. Kanazawa, J.-H. Kim, D. S. Inosov, J. S. White, N. Egetenmeyer, J. L. Gavilano, S. Ishiwata, Y. Onose, T. Arima, B. Keimer, and Y. Tokura, *Phys. Rev. B* **86**, 134425 (2012).
- [13] O. L. Makarova, A. V. Tsvyashchenko, G. Andre, F. Porcher, L. N. Fomicheva, N. Rey, and I. Mirebeau, *Phys. Rev. B* **85**, 205205 (2012).
- [14] N. Kanazawa, J. S. White, H.M. Rønnow, C. D. Dewhurst, D. Morikawa, K. Shibata, T. Arima, F. Kagawa, A. Tsukazaki, Y. Kozuka, M. Ichikawa, M. Kawasaki, and Y. Tokura, *Phys. Rev. B* **96**, 220414(R) (2017).
- [15] N. Kanazawa, A. Kitaori, J. S. White, V. Ukleev, H.M. Rønnow, A. Tsukazaki, M. Ichikawa, M. Kawasaki, and Y. Tokura, *Phys. Rev. Lett.* **125**, 137202 (2020).
- [16] B. Binz, A. Vishwanath, and V. Aji, *Phys. Rev. Lett.* **96**, 207202 (2006).

Polarization Analyzed Imaging with a Neutron Grating Interferometer

M. Strobl

J. Valsecchi

Paul Scherrer Institut (PSI)
5232 Villigen PSI, Switzerland

Abstract

Neutron grating interferometry has been pioneered at PSI in 2006, when it was established as a new, superior means for differential phase contrast imaging. A short time later, however, it could be shown, that it enables yet another imaging modality, referred to as dark-field contrast imaging. Dark-field contrast imaging gained significantly more importance and enabled to detect local microstructural features based on the provided sensitivity to small-angle scattering. In particular dark-field contrast neutron imaging proved sensitive to ferromagnetic domains and allowed to directly depict the domain wall structure of bulk ferromagnetic materials with large domains as e.g. in grain oriented electric steels. Subsequently grating interferometers were installed at many state-of-the-art neutron imaging instruments around the world and a vivid and fast developing field of research has been established leading to significant progress in recent years. Our latest achievement after introducing quantitative analyses of local small-angle scattering in neutron dark-field contrast imaging is the establishment of polarized and polarization analyzed neutron grating interferometry. The latter enabled us to not only measure sub-micron beam splitting in a centimeter sized beam in a Stern-Gerlach

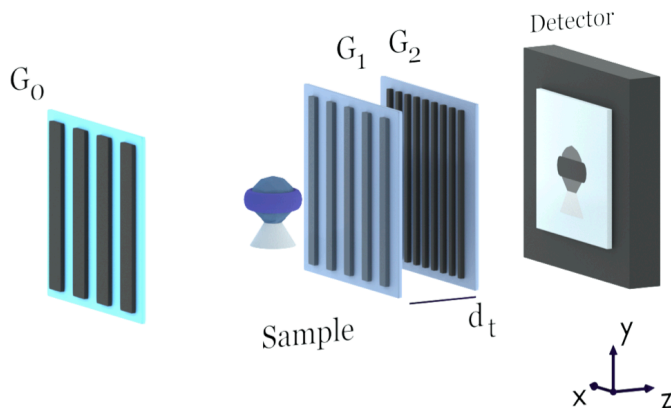


Figure 1

Schematic of a classic neutron grating interferometer setup installed downstream from a neutron source and an energy selector (optional) consisting of a source grating G_0 , a phase grating G_1 , an analyzer grating G_2 and a neutron detector. The parameter d_t is the distance between $G_1 - G_2$. One of the gratings, usually G_2 , is stepped in x direction during the acquisition routine over a full period. The neutron beam propagation is along the z -axis.

type experiment, but to also clarify eventually the origin of magnetic dark-field contrast.

Intro

Neutron grating interferometry is generally based on the use of a Talbot-Lau grating interferometer consisting of three gratings G_0 , G_1 and G_2 , two absorption (G_0 , G_2) and one phase grating (G_1)¹, as depicted in Figure 1. The so-called source grating G_0 creates a partially coherent beam consisting initially of a number of separated beams passing through the absorption grating. The coherence of these beams, based on the period and duty cycle of G_0 and its distance to G_1 is chosen such that the subsequent $\pi/2$ phase grating G_1 is illuminated coherently and, thus, creates an interference pattern. Corresponding to the Talbot effect this interference leads to self-imaging of the grating structure at frac-

tional Talbot distances^{2,3}. Thus, the geometry of G_0 and its distance to G_1 has to be chosen also such, that the self-images created by the individual coherent beams formed by G_0 add constructively at the chosen fractional Talbot distance (d_t) at which the interference is to be detected. As the periods of G_1 and, hence, also the interference pattern, are normally chosen to be in the micrometer range another absorption grating G_2 , with the period p of the modulation pattern, is utilized to resolve the self-image. Considering that the beam modulation pattern serves to resolve small angular beam deviations induced by a sample, the micrometer sized periods are required to be sensitive to differential phase effects. The approach with an analyzer grating G_2 implies, that one grating has to be scanned, in order to resolve the beam modulation of the interference pattern, as shown in Figure 2. This process is commonly referred to as phase

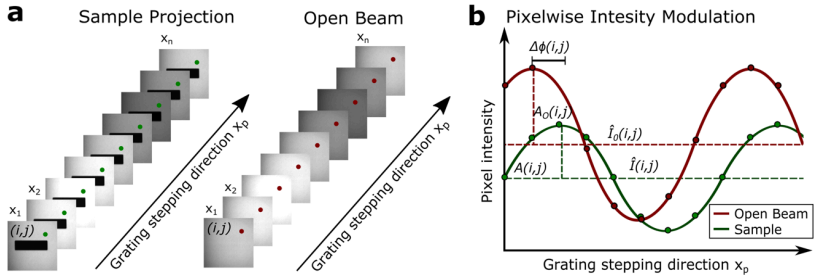


Figure 2

Phase-stepping routine for data acquisition of a grating interferometer experiment. a) A set of n -individual images with sample as well as without sample at various grating steps x_p are recorded. Green indicates the stack of recorded images for the sample projection and red the open beam respectively. The dot marker depicts the (i, j) -pixel on the matrix detector. b) The resulting intensity modulation for the (i, j) -pixel, green and red dots for the sample projection and the open beam respectively, as a function of the grating steps x_p and the corresponding sinusoidal fits. $\hat{I}(i, j)$ and $\hat{I}_0(i, j)$ are the mean values obtained after the stepping procedure with and without the sample, respectively. $A(i, j)$ and $A_0(i, j)$ are the amplitude values with and without the sample. $\Delta\phi(i, j)$ is the difference between the phase of the open beam stepping and the phase of the stepping with sample, while taking phase wrapping into account.

stepping and provides a modulation pattern for each individual pixel of an imaging detector placed downstream of G_2 . Utilizing an imaging detector and an initially pinhole collimated beam, with the pinhole generally upstream of G_0 , allows analyzing the effect of a sample on the modulation pattern locally for each sample and thus spatially resolved for the projection of the sample.

The effects of the sample can influence the three parameters of the beam modulation (here expressed for an individual pixel of the imaging detector)

$$I = \hat{I} + A \sin(2\pi x_p / p + \phi)$$

namely \hat{I} , defining the beam attenuation through \hat{I}/\hat{I}_0 , where \hat{I}_0 is the open beam equivalent, the amplitude A and the modulation

phase ϕ . x_p indicates the phase stepping. The phase ϕ deviates from zero when the beam is deflected and the specific angle of deflection can be calculated from the spatial phase $\phi = \phi_p / 2\pi$ and the distance of the object from the analyzer grating G_2 , typically a few centimeters, in particular if the sample is placed between G_1 and G_2 . Periods of a few micrometers and distances of a few centimeters result in an angular resolution of milli- to microradians, well suited to resolve refraction effects and subsequently quantify local phase shifts by the sample, thus allowing phase imaging. Finally, and most importantly, the amplitude A when correlated to the average intensity \hat{I} provides a measure of the visibility as

$$V = A/\hat{I} = (I_{\max} - I_{\min}) / (I_{\max} + I_{\min}).$$

Amplitude is lost, when within one pixel, or generally within one period, when different beam deflections are contributing. This is the case especially for small-angle neutron scattering (SANS), where a symmetric angular redistribution of the beam is induced.

Modulation visibility is lost according to a convolution of the modulation pattern with the small-angle scattering pattern⁴ and assuming the symmetry of small-angle scattering one can write⁵.

$$V(\xi) = V_0(\xi) \int dq S(q) \cos(\xi q)$$

where V_0 is the open beam visibility, q is the modulus of the scattering vector (in x -direction) and ξ being the correlation length probed with specific instrumental parameters according to

$$\xi = \lambda L_s / p$$

where λ is the wavelength and L_s the sample to G_2 distance (for a sample placed between G_1 and G_2).

$S(q)$ is the small-angle scattering function, which can be written as Fourier transform of the

real space correlation function G of the scattering structure as

$$S(q) = \int_{-\infty}^{+\infty} d\xi G(\xi) \cos(\xi q).$$

It has to be noted, that the one-dimensional modulation enables scattering resolution only in one direction (x -direction), i.e. perpendicular to the grating lines. Thus, G and S have to be assumed projected functions, similar to the situation in a Bose-Hart camera for ultra-SANS (USANS).

It can, thus, be shown, that the measurement establishes a back transformation of scattering from reciprocal space to real space according to

$$V(\xi) / V_0(\xi) = \int dq S(q) \cos(\xi q) = G(\xi).$$

Taking into account the total scattering probability and multiple scattering one arrives at⁵

$$V(\xi) / V_0(\xi) = e^{\Sigma t(G(\xi)-1)}$$

which allows to extract quantitative local microstructure information from the dark-field contrast signal when scanning ξ ⁶. This has

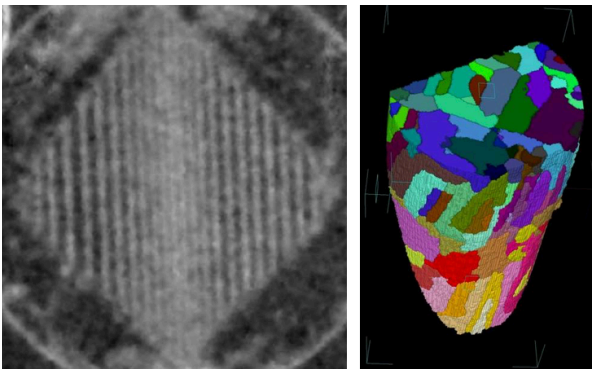


Figure 3

First neutron dark-field contrast image of magnetic domains⁸ and extension to 3D: first observation of magnetic domain structure in bulk ferromagnet⁹.

allowed numerous studies combining macroscopic imaging resolution with microscopic structure resolution of neutron grating interferometry triggering the development of numerous grating interferometer designs and beam modulation techniques to extend the efficiency and probed correlation length range⁷.

However, care has to be taken, as dark-field signal also arises for example due to resolution limitations e.g. at edges displaying a steep gradient of differential phase contrast or from phase objects beyond direct spatial resolution. A very special case are magnetic structures and in particular magnetic domain walls, the detection of which established one of the dominating use cases of dark-field contrast neutron imaging. In general, such studies are performed with a non-polarized neutron beam and the obtained dark-field contrast was initially argued to be based on

‘decoherence’, better expressed as local degradation of coherence, induced to the beam by domain wall structures (“decoherence imaging”)⁸.

In order to shed light on the contrast mechanism and to eventually enable quantitative microstructural studies of magnetic materials we introduced first polarized neutrons and subsequently also polarization analyses to Talbot Lau grating interferometric neutron imaging.

Experimental

A polarized neutron grating interferometer set-up was established at the BOA beamline of SINQ at PSI. The beamline provides a cold polarized beam from a polarizing bender installed in the shielding monolith of SINQ. In order to conserve and manipulate the beam polarization a guide field was installed from

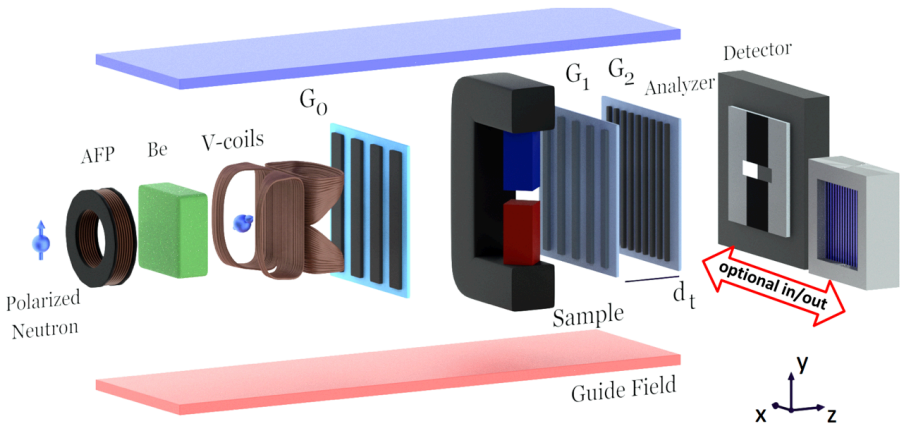


Figure 4

Polarized and optionally polarization analyzed neutron grating interferometer for imaging applications¹⁰

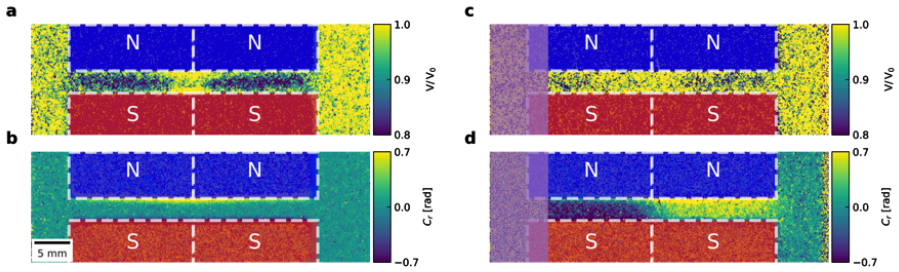


Figure 5

Spatial beam splitting results¹⁰. (a,b) Dark-field image DFI and differential phase contrast image DPCI of the magnetic field prism measured without the spin analyzer, top and bottom respectively. (c,d) Dark-field image DFI and differential phase contrast image DPCI of the magnetic field prism measured with the spin analyzer in place. Where C_r is the relative phase. The North (N) and South (S) square-shaped pole shoes are depicted in blue and red, respectively. The shaded areas show the blind region lying outside the field of view of the analyzer. a-d) share the same size scalebar. e) Illustration of the corresponding effect on the as measured interference pattern $|\uparrow\rangle + |\downarrow\rangle$ (red curve), according to an ideal open beam modulation (I_0) (blue curve) and the thus assumed individual and separate interference patterns of the spin-up $|\uparrow\rangle$ (orange dashed line) and the spin-down $|\downarrow\rangle$ state (green dashed line) in the plateau regions where the dark-field contrast is quantified to $V/V_0 = 0,87$, while no phase contrast is measured. The corresponding effect on the interference pattern of only the spin-up $|\uparrow\rangle$ (orange line dashed), according to an ideal open beam modulation (I_0) (blue curve) in the plateau regions where $C_r = 0,5$ rad, while the dark-field contrast is quantified to $V/V_0 = 1$

beam exit to the detector, hosting an adiabatic fast passage spin flipper (AFP) a pair of V-coils as well as a Be-filter and an optional solid-state bender-type polarization analyzer (Figure 4)¹⁰. The V-coil system allows to turn the initial vertical polarization into the horizontal plane through an adiabatic transition.

Images of a magnetic field between the square-shaped pole shoes of an iron yoke aligned vertically, i.e. perpendicular to the incident spin polarization, were acquired. The

square cross section was aligned with the diagonal in beam direction, thus, creating a centrally symmetric inclined gradient field across the beam. In the presence of the magnetic field gradient and without the polarization analyzer in the beam a significant dark-field contrast signal is recorded on both sides of the symmetric sample arrangement, but no phase contrast, as shown in Figure 5a and 5b, respectively. That no differential phase effect is measured, i.e. $\phi = 0$, contrasts previously

reported results¹¹ where the neutron spins coupled adiabatically to the same sample field. The adiabatic coupling is prevented this time by the rotation of the spin by the V-coil arrangement in order to precess in the guide field aligned parallel to the sample field. The measured dark-field contrast could be quantified to be $V/V_0 = 0.87$.

A second measurement is performed with the polarization analyzer in placed in the beam. The analyzer is aligned in a vertical configuration that only transmits spin-up neutrons. In contrast to the first measurement, full visibility is regained, i.e. $V/V_0 = 1$, while a significant phase contrast is recorded with $\phi = \pm 0.5$ rad. The results are juxtaposed to the first measurement in Figure 5c,d. The measured phase shift of the interference pattern corresponds to a spatial beam shift of $0.318 \mu\text{m}$, as depicted in Figure 5(e).

This value smoothly transitions to zero at the edges and at the center similar to the dark-field contrast I the first measurement. The average intensity is half compared to the initial measurement which corresponds well with the removal of neutrons with opposite spin state and the assumption of an equal distribution between both states according to the initially perpendicular alignment of field and polarization.

The results are indeed compatible with the quantum mechanical expectation of a transversal split of the spin-up $|\uparrow\rangle$ and spin-down $|\downarrow\rangle$ states at the inclined field regions. The results further imply that both spin states create independent interference patterns with full visibility exhibiting a spatial phase shift according to the induced differential phase. This is underlined in the second measurement, where one spin state is suppressed,

and thus the corresponding visibility and phase shift of the other can be measured directly.

In the first measurement, however, the superposition of the two separate intensity modulations for the two separate spin states, with symmetrically opposite phase offsets is suited to explain the visibility loss through additive superposition of the two independent intensities represented by the dark-field contrast in the corresponding regions.

The recorded phase shift $\phi = \pm 0.5$ rad corresponds to a transversal split of the two spin states of $0.64 \mu\text{m}$ at G_2 . In accordance with the assumed intensity superposition probed in the first measurement this calculation returns a relative visibility of $V/V_0 = 0.87$ in agreement with the measurement result. The superposition of the two symmetrically but oppositely shifted interference patterns implies a vanishing resulting phase shift again in accordance with the measurement.

It is, thus, demonstrated that the spin states parallel and antiparallel to the precession field are split transversally due to opposite refraction angles at the magnetic phase object, and both wave functions independently create interference patterns at the fractal Talbot distance of G_2 . These coherent interference patterns are however offset according to their transversal splitting. This offset of intensity modulations leads to a related loss of visibility due to an additive superposition of intensities. The measurement of the dark-field contrast resembles a Stern-Gerlach experiment where the transversal split of spin states of the order of 640 nm is measured without actual beam splitting of a centimeter sized beam.

The experiments further confirm that the individual wave functions of the split spin states, have conserved coherence and display no visibility loss of the interference pattern within the accuracy of the measurement, but only a phase shift according to the differential phase effect. Therefore, the magnetic dark-field contrast signal has been successfully decomposed to phase contrast of separate spin states. It can therefore be assumed, that dark-field contrast measured with an unpolarized beam at strong magnetic field gradients, as often utilized to visualize

magnetic domain walls, is based on the effect of split spin-up and spin-down states, based on the magnetic differential phase effect, and instead of a loss of coherence an intensity addition of shifted interference patterns causes the loss of visibility.

Furthermore, the introduced setup of a neutron grating interferometer for polarized neutrons with optional polarization analysis could be shown to bear the capability to measure spatially resolved spin analyzed magnetic small-angle scattering based on the dark-field contrast imaging method¹².

References

- [1] Pfeiffer, F. et al. Neutron phase imaging and tomography. *Phys. Rev. Lett.* **96**, 215505 (2006).
- [2] Case, W. B., Tomandl, M., Deachapunya, S. & Arndt, M. Realization of optical carpets in the Talbot and Talbot-Lau configurations. *Opt. Express* **17**, 20966 (2009).
- [3] Harti, R. P. et al. Visibility simulation of realistic grating interferometers including grating geometries and energy spectra. *Opt. Express* **25**, 1019 (2017).
- [4] Strobl, M. et al. Neutron dark-field tomography. *Phys. Rev. Lett.* **101**, 123902 (2008).
- [5] Strobl, M. General solution for quantitative dark-field contrast imaging with grating interferometers. *Sci. Rep.* **4**, 7243 (2014).
- [6] Strobl, M. et al. Wavelength-dispersive dark-field contrast: micrometre structure resolution in neutron imaging with gratings. *J. Appl. Crystallogr.* **49**, 569–573 (2016).
- [7] Strobl, M. et al., Small Angle Scattering in Neutron Imaging—A Review. *J. Imaging* **3** (2018) 64
- [8] Grünzweig, C. et al. Neutron decoherence imaging for visualizing bulk magnetic domain structures. *Phys. Rev. Lett.* **101**, 025504 (2008).
- [9] Manke, I. et al. Three-dimensional imaging of magnetic domains. *Nature Commun.* **1**, 125
- [10] Valsecchi, J. et al. Decomposing magnetic dark-field contrast in spin analyzed Talbot-Lau interferometry - a Stern-Gerlach experiment without spatial beam splitting. *Phys. Rev. Lett.* **126**, 070401 (2021)
- [11] Valsecchi, J. et al. Visualization and quantification of inhomogeneous and anisotropic magnetic fields by polarized neutron grating interferometry. *Nat. Commun.* **10**, 3788 (2019).
- [12] Valsecchi, J. et al. Towards spatially resolved magnetic small-angle scattering studies by polarized and polarization-analyzed neutron dark-field contrast imaging. *Scientific Reports* **11**(1): 8023 (2021)

Announcements

SNSS/SGN Members

Presently the SGN/SNSS has 203 members. New members can register online on the SGN/SNSS website: <http://sgn.web.psi.ch>

New strategy paper for neutron science in Switzerland

In spring 2021, the SNSS/SGN has published a strategy for neutron science in Switzerland together with the involved facilities and the community of researchers using neutrons. Together with other Road Map publications, the Neutron Science Road Map 2025-2028 has been published on the platform of the Swiss Academy of Sciences (SCNAT) and it can be downloaded on the SNSS page: <https://sgn.web.psi.ch/sgn/strategy.html>

SNSS/SGN Annual Member Fee

The SGN/SNSS members are kindly asked to pay their annual member fees. At the general assembly 2013 of the society, the fee has been increased from CHF 10 to **CHF 20**. It can be paid either by bank transfer or in cash

during your next visit at PSI. The bank account of the society is accessible for both Swiss national and international bank transfers: Postfinance: 50-70723-6 (BIC: POFICHBE), IBAN: CH39 0900 0000 5007 0723 6.

The SGN/SSSN is an organisation with tax charitable status. All fees and donations paid to the SGN/SSSN are **tax deductible**.

PSI Facility News

Recent news and scientific highlights of the three major PSI user facilities SLS, SINQ and μ S can be found in the quarterly electronic newsletter available online under: <https://www.psi.ch/science/facility-newsletter>

News from SINQ

The SINQ Upgrade has been finished. A few instruments have not yet joined user operation: DMC receives a new ^3He detector and commissioning is planned for the second user cycle of 2021. The reflectometer AMOR will be commissioned in 2022. While the new Selene optics for AMOR was installed during

the SINQ upgrade, the secondary instrument is not yet finished.

In collaboration with the Laboratoire Léon-Brillouin (Saclay, France) the instrument SANS-LLB is being installed at SINQ. Commissioning is planned for the first cycle in 2022, and SANS-LLB is planned to join the user program in the second cycle of 2022.

While many experiments in 2020 and in the first cycle of 2021 have been affected by the Corona pandemic, most experiments in the second cycle of 2021 have taken place with presence of the users.

Please visit the page <https://www.psi.ch/sinq/call-for-proposals> to obtain the latest information about beam cycles and the availability of the neutron instruments.

Registration of publications

Please remember to **register all publications either based on data taken at SINQ, SLS, SpS or having a PSI co-author** to the Digital Object Repository at PSI (DORA):

www.dora.lib4ri.ch/psi/

Follow the link 'Add Publication'.

Open Positions at SINQ and ILL

To look for open positions at SINQ or ILL, have a look at the following webpages:

<https://www.psi.ch/pa/stellenangebote>

<https://www.ill.eu/careers/all-our-vacancies/?L=0>

PhD positions at ILL

The PhD program of the Institut Laue-Langevin, ILL, is open to researchers in Switzerland. Consult the page <https://www.ill.eu/careers/all-our-vacancies/phd-recruitment> for information on the PhD program of ILL or get in contact with the managers of the program using the email address phd@ill.fr. The Swiss agreement with the ILL includes that ILL funds and hosts one PhD student from Switzerland.

Young Scientist Prize 2021 of the Swiss Neutron Science Society, sponsored by SwissNeutronics

The Young Scientist Prize 2021 of the society is awarded to young researchers for their outstanding achievements using neutron ra-

diation in the framework of their PhD theses. The prize is awarded at the virtual Annual Assembly of the society, 26.11.2021.

The prize of 2021 is split and awarded to:

Dr. Jakob Lass

in recognition of his outstanding work on "Neutron scattering and data treatment for camea-like back-ends."

and to:

Dr. Jacopo Valsecchi

in recognition of his outstanding work on "Polarized neutron imaging and grating interferometry for visualization and quantification of magnetic systems."

Young Scientist Prize 2022 of the Swiss Neutron Science Society, sponsored by SwissNeutronics

Call for Nominations

The Swiss Neutron Science Society hereby announces the call for nominations for the 9th Young Scientist Prize of the Swiss Neutron Science Society.

In 2022, the prize will be awarded to a young scientist in recognition of a notable scientific achievement in the form of a PhD thesis that was awarded within two years of the announcement of the call. The science should include the use of neutron radiation, and eligible nominees should have a clear affiliation with Swiss neutron science (be member of the Swiss Neutron Science Society, be based in Switzerland, or have conducted experiments at Swiss neutron facilities). The PhD must have been awarded within two years of the announcement of this call. The prize amounts to 1'000 CHF and is sponsored by SwissNeutronics.

Nominations for the prize should be submitted to the Swiss Neutron Science Society: sgn@psi.ch

The deadline for nominations is February 28th, 2022.

Nominations should include:

- Nomination letter including the motivation for the award
- CV and publication list of the nominee
- Digital copy of the nominated work (PhD thesis)
- Letter documenting the acceptance of the nomination by the nominee
- Letters of support from authorities in the relevant field are accepted

Nominations for the prize will be treated confidentially. Nominations for the prize will be evaluated by a selection committee appointed by the board of the Swiss Neutron Science Society. The nominations will be acknowledged, but there will be no further communication. More information is available online: https://sgn.web.psi.ch/sgn/young_scientist_prize.html

Conferences and Workshops 2022

An updated list with online links can be found here:
<http://www.psi.ch/useroffice/conference-calendar>

January 2022

LINXS Event - Workshop: An Introduction to surface x-ray and neutron scattering techniques

January 10, 2022, online

LINXS Related Event - Nordic Workshop on Scattering from Soft Matter

January 10-11, 2022, online

SXNS16: 16th International Conference on Surface X-ray and Neutron Scattering

January 11-14, 2022, Lund, Sweden

Third Pan African Conference on Crystallography

January 17-22, 2022, Nairobi, Kenya

Joint DESY Photon Science and European XFEL Users' Meeting

January 24-28, 2022, Hamburg, Germany

ERIC Forum Meeting 2022

January 26-27, 2022, online

February 2022

French-Swiss Meeting SANS for Soft Matter

February 2-3, 2022, Strasbourg, France

SLS 2.0 User Information Workshop

February 28, 2022, online

HERCULES European School 2022

February 28 - April 1, 2022, Grenoble, France

March 2022

RACIRI School 2022

March 12-19, 2022, Sweden

APS March Meeting 2022

March 14-18, 2022, Chicago, USA

April 2022

LINXS Partner Event - 18th Food Colloids conference: Structure, Dynamics and Function

April, 10-13, 2022, Lund, Sweden

SICT 2022: International Conference on Surfaces, Interfaces and Coatings Technologies
April 27-29, 2022, Barcelona, Spain

May 2022

LEAPS meets Quantum Technology Conference

May 16-20, 2022, Isola d'Elba, Italy

QENS/WINS 2022

May 23-27, 2022, San Sebastian, Spain

MLZ Conference 2022: Neutrons for mobility

May 31 - June 3, 2022, Lenggries, Germany

June 2022

Bombannes Summer School 2022

June 20-28, 2022, Carcan-Maubuisson (Gironde), France

August 2022

ICNS 2022: 12th International Conference on Neutron Scattering

August 21-25, 2022, Buenos Aires, Argentina

15th International Conference on Muon Spin Rotation, Relaxation and Resonance

August 28 - September 2, 2022, Parma, Italy

September 2022

Diffusion Fundamentals IX

September 21-24, 2022, Krakow, Poland

October 2022

Third ESS and ILL European Users Meeting

October 5-7, 2022, Lund, Sweden

PSI 2022: 6th Workshop on "Physics of fundamental Symmetries and Interactions"

October 16-21, 2022, PSI Villigen, Switzerland

Editorial

Editor

Swiss Neutron Science Society

Board for the Period 2019 – 2021:

President

Prof. Dr. H. Ronnow
henrik.ronnow@epfl.ch

Board Members

Prof. Dr. M. Strobl
markus.strobl@psi.ch

PD Dr. K. Krämer
karl.kraemer@dcb.unibe.ch

PD Dr. U. Gasser (secretary)
urs.gasser@psi.ch

Honorary Members

Prof. Dr. W. Hälg, ETH Zürich (†)

Prof. Dr. K. A. Müller
IBM Rüschlikon and Univ. Zürich

Prof. Dr. A. Furrer
ETH Zürich and Paul Scherrer Institut

Auditors

Dr. M. Zolliker, Paul Scherrer Institut
Prof. Dr. Florian Piegsa, Univ. Bern

Address

Sekretariat SGN/SSSN/SNSS
c/o Paul Scherrer Institut
WLGA/018
5232 Villigen PSI, Switzerland
phone: +41 56 310 46 66
fax: +41 56 310 32 94
<http://sgn.web.psi.ch>

Bank Account

Postfinance: 50-70723-6 (BIC: POFICHBE)
IBAN: CH39 0900 0000 5007 0723 6

Printing

Paul Scherrer Institut
Circulation: 1600
2 numbers per year

Copyright

SGN/SSSN/SNSS and the respective authors

Swiss Neutron Science Society

Sekretariat SGN/SSSN
WLGA/018
Paul Scherrer Institut
5232 Villigen PSI, Switzerland



Join the Swiss Neutron Science Society...

to support all science using neutron radiation in Switzerland.

The Swiss Neutron Science Society is open to everybody interested in neutron scattering and research using neutron radiation in general.

The annual membership fee is CHF 20.-, but the membership is free for Bachelor-, Master-, and PhD-students.

Send an email to sgn@psi.ch to join.